

## Article

# Multifunctional Control Technique for Grid-Tied Hybrid Distributed Generation System Taking into Account Power Quality Issues

Sohaib Abdeslam Boulanouar <sup>1,\*</sup>, Ameer Miloud Kaddouri <sup>1</sup>, Abdellah Kouzou <sup>1,2</sup>, Amar Benaissa <sup>1</sup>, Ali Teta <sup>1</sup>, Ahmed Hafaifa <sup>1,2</sup>, Ralph Kennel <sup>3</sup> and Mohamed Abdelrahem <sup>3,4,\*</sup>

<sup>1</sup> Laboratory of Applied Automation and Industrial Diagnostics (LAADI), Faculty of Science and Technology, Ziane Achour University, Djelfa 17000, Algeria; amkaddouri@yahoo.fr (A.M.K.); kouzouabdellah@ieee.org (A.K.); benaissa\_am@yahoo.fr (A.B.); ali.teta@univ-djelfa.dz (A.T.); a.hafaifa@univ-djelfa.dz (A.H.)

<sup>2</sup> Electrical and Electronics Engineering Department, Nisantasi University, Istanbul 34398, Turkey

<sup>3</sup> Chair of High-Power Converter Systems, Technical University of Munich (TUM), 80333 Munich, Germany; ralph.kennel@tum.de

<sup>4</sup> Department of Electrical Engineering, Assiut University, Assiut 71516, Egypt

\* Correspondence: s.boulanouar@univ-djelfa.dz (S.A.B.); mohamed.abdelrahem@tum.de (M.A.)

**Abstract:** This paper proposes a new multifunctional control technique for a grid-connected hybrid distributed generation system composed of a photovoltaic system and a wind power system based on a voltage source converter (VSC). Indeed, aside from the generation and the injection of energy into the grid, the proposed system deals with power quality issues caused by harmonics generated by non-linear loads in order to keep the source current uncontaminated. The VSC serves to first ensure that the power generated from the hybrid renewable energy source is fed to the utility grid and acts as a shunt active power filter in case an abnormal increase in the THD of the source current above the standard permissible values is detected due to the non-linear load connection. The two sources of the hybrid system are connected to a common DC bus to simplify the control and reduce the cost of the system, and a maximum power point tracking controller is used for both sources. The major advantage of this novel proposed multifunctional control technique is its ability to inject harvested power into the grid while simultaneously ensuring the compensation of the harmonics and reactive power. The proposed multifunctional control technique is validated through an extensive simulation analysis using MATLAB/Simulink.

**Keywords:** harmonic elimination; power quality; renewable energy; hybrid system



**Citation:** Boulanouar, S.A.; Kaddouri, A.M.; Kouzou, A.; Benaissa, A.; Teta, A.; Hafaifa, A.; Kennel, R.; Abdelrahem, M. Multifunctional Control Technique for Grid-Tied Hybrid Distributed Generation System Taking into Account Power Quality Issues. *Energies* **2023**, *16*, 6565. <https://doi.org/10.3390/en16186565>

Academic Editor: Abu-Siada Ahmed

Received: 17 August 2023  
Revised: 4 September 2023  
Accepted: 7 September 2023  
Published: 12 September 2023



**Copyright:** © 2023 by the authors. Licensee MDPI, Basel, Switzerland. This article is an open access article distributed under the terms and conditions of the Creative Commons Attribution (CC BY) license (<https://creativecommons.org/licenses/by/4.0/>).

## 1. Introduction

Recently, as a result of the environmental issues caused by the consumption of unclean forms of energy and the economic trends of many countries, the exploitation of renewable energy sources has been rapidly increasing. This is due to the fact that these sources have several advantages, for example, they produce clean electrical energy with zero carbon emissions, they do not require high maintenance costs, and, most importantly, the energy can be harvested freely [1]. Therefore, this field is attracting a growing number of scientific research studies [2,3]. In addition, renewable energy sources can be combined to achieve more efficiency and profitable energy [4–6].

It is obvious that to benefit from the power produced by distributed generation (DG) sources in grid-tied applications, power converters are used to ensure the connection of the DG sources and control over the flow of the produced power into the grid [7–9]. However, it is well known that the grid suffers from the proliferation of harmonic contamination caused by nonlinear loads such as transformers, power electronic equipment, and arcing devices [10,11]. These harmonics have a significant impact on the quality of the

power delivered to the loads, which are connected to the same point of common coupling (PCC) [12,13].

Conventionally, in order to eliminate the effect of current harmonics and ensure power factor correction, several traditional techniques have been used, such as passive filters [14,15]. Despite their ease of implementation and low cost, they have numerous drawbacks, such as their large size [16] and their vulnerability to resonance phenomena [17].

Instead, other solutions have been developed to overcome the shortcomings of traditional techniques, including active power filters (APFs), which can be classified according to their structure into series, shunt, or hybrid topologies [18]. The shunt active power filter (SAPF) topology is widely used due to its simple topology and efficient operation [19,20].

Generally, shunt active power filters are based on voltage source inverters that interface a capacitor on the DC side, where they are connected to the point of common coupling via output filters. Indeed, the main role of the SAPF is to inject compensating currents to ensure the suppression of harmonics and the reactive components of the currents generated by nonlinear and reactive loads [21].

In the literature, several researchers have proposed different control techniques dedicated to grid-tied hybrid distributed generation systems for power injection and power quality enhancement. In [22], a review of the topologies and control strategies of multifunctional grid-connected inverters (MFGIs) was carried out. In [23], the authors offer large solutions to power quality issues using different topologies and control techniques for shunt active power filters integrated with renewable energy systems. In [24], a hybrid energy system (HES) integrated with a shunt active power filter was proposed to eliminate the current harmonics in a grid. In [25], the authors focused on the quality of the injected current by proposing a reference signal generation algorithm. In [26], an effective control strategy was proposed for a multifunctional grid-tied inverter (MFGTI) to enhance the power quality in the microgrid. In [27,28], a comparative study was carried out between an intelligent controller and a nonlinear controller for a three-phase inverter connected to hybrid renewable energy source (HRES) systems.

The dynamic of the power transferred to the grid depends mostly on the load current profile, the DG systems, and the grid. Consequently, this permits a simultaneous adjustment of the transferred power and the related current injected into the grid according to any eventual variations that may occur within the aforementioned systems. To ensure such dynamic behavior, a novel multifunctional control technique scheme is proposed that is able to control the injected current under different grid conditions.

The aim of this work is to investigate a novel multifunctional control technique used in hybrid distributed generation systems, which include photovoltaic and permanent magnet synchronous generator (PMSG) wind turbine systems. This configuration is based on a common DC bus instead of an AC bus to integrate these renewable energy sources for the purpose of simplifying and reducing the cost of the system. In its normal mode, the inverter ensures the transfer of the power generated by the hybrid system to the utility grid. When an abnormal increase in the THD of the source current above the permissible value is detected, which mainly occurs to the connection of a nonlinear load to the grid, causing a significant propagation of harmonic components, the developed system further acts as a shunt active power filter to ensure the compensation of these generated harmonics, in addition to improving the power factor by compensating the reactive component of the current.

This paper is structured as follows: Section 1 provides a detailed description of the proposed configuration. Section 2 discusses the proposed control system, wherein the current control for both cases and the reference current identification strategies are demonstrated well. Section 3 presents the simulation results, which prove the performance effectiveness of the proposed configuration by comparing a backstepping controller to a classic hysteresis controller, and finally, this paper ends with general conclusions.

## 2. System Description

Figure 1 illustrates the overall structure of the hybrid distributed generation system based on the proposed multifunctional control technique, which includes two renewable energy sources, a photovoltaic system and wind energy conversion system (WECS), connected to the grid. The WECS consists of a three-blade wind turbine based on a permanent magnet synchronous generator (PMSG) connected to a full-bridge diode rectifier, which is connected to a DC/DC boost converter to control the extracted electric power and its transfer to the DC bus. The PV generator is connected to the common DC bus in parallel with the WECS through a second DC/DC boost converter. The DC bus is connected to the grid by means of a voltage source inverter (VSI) through a first-order coupling filter.

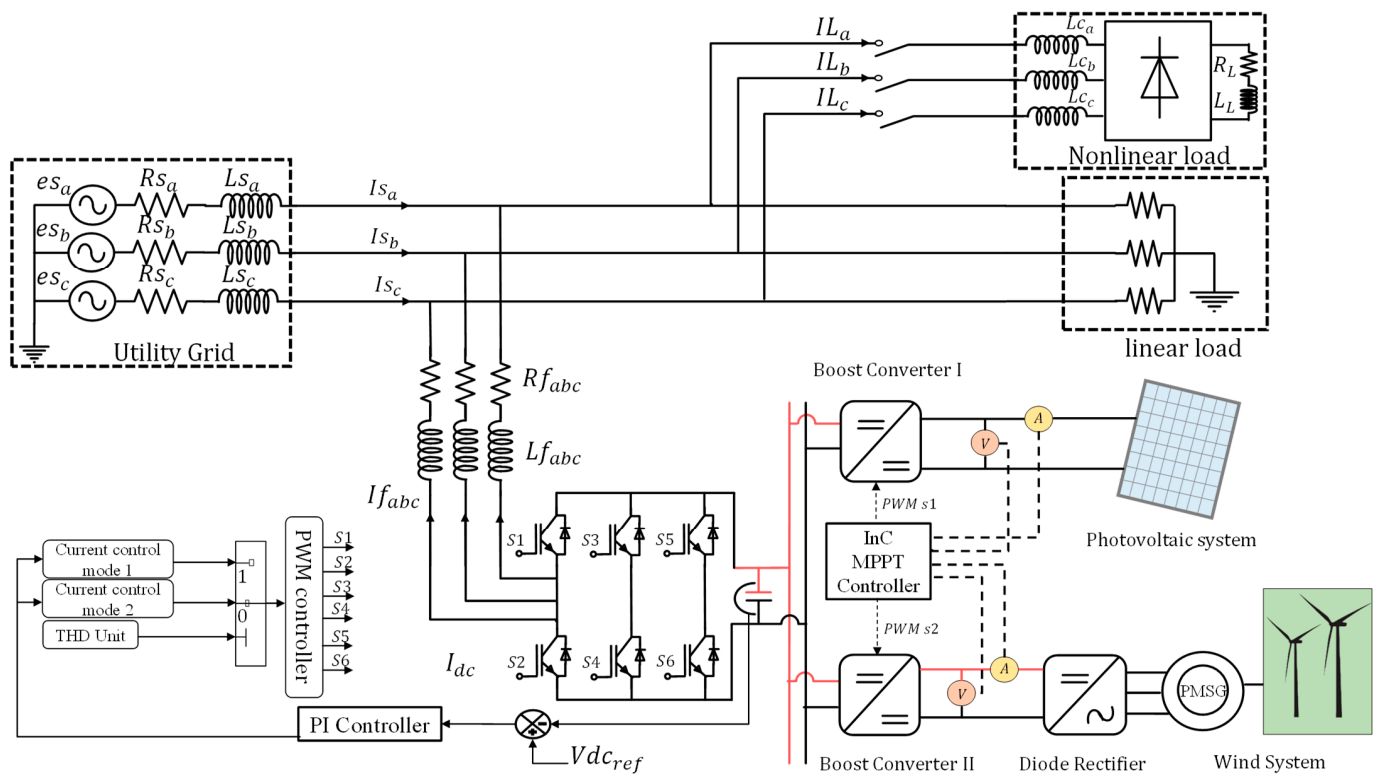


**Figure 1.** The overall scheme of the proposed system.

In the first operating mode, the proposed system ensures that the power generated by the hybrid distributed source is fed into the utility grid. While in the second mode, the designed system works as an active power filter to reduce the harmonic current and compensate for the reactive power when an abnormal rise in the THD of the source current is found. This unanticipated power quality degradation could be caused by the sudden connection of nonlinear loads or reactive loads to the grid.

Regarding the control unit of the DC side, the two sources are controlled via boost converters to track the maximum power point using an MPPT technique based on an incremental conductance (InC) strategy for both photovoltaic and wind energy systems. In addition, a PI controller is used to keep the voltage stable across the DC-link despite the abrupt environmental conditions. The synchronous reference frame (SRF) theory is adopted in the second operating mode under weak grid conditions to identify harmonic components.

Finally, the proposed non-linear backstepping approach that controls the injected current is compared with a hysteresis controller in both operating modes.

## 2.1. The Stand-Alone System Modeling

### 2.1.1. PV System Modeling

The basic equivalent circuit of the PV cell consists of a single diode model, as shown in Figure 2.

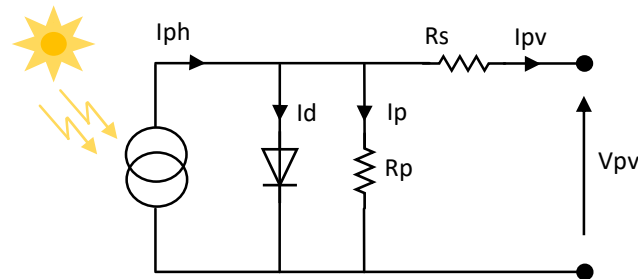


**Figure 2.** Equivalent circuit of the PV cell.

The expression representing the output current of a photovoltaic (PV) cell is formulated as follows [29]:

$$I_{pv} = I_{ph} - I_d - I_p \quad (1)$$

where  $I_{ph}$ ,  $I_d$ , and  $I_p$  are the photocurrent, diode current, and leakage current in parallel resistance, respectively. The photocurrent and the diode current can be expressed as follows [29]:

$$I_{ph} = \left( \frac{G}{G_{ref}} \right) \cdot (I_{ph,ref} + \mu_{sc} \cdot \Delta T) \quad (2)$$

where  $G$  is the irradiance ( $\text{W}/\text{m}^2$ ),  $G_{ref}$  and  $I_{ph,ref}$  are the references of the irradiance and photocurrent at STC,  $\Delta T$  is the difference in temperature, and  $\mu_s$  is the short-circuit coefficient temperature ( $\text{A}/\text{K}$ ).

$$I_d = I_0 \left[ \exp \left( \frac{V_{pv} + R_s \cdot I_{pv}}{A \cdot N_s \cdot V_t} \right) - 1 \right] \quad (3)$$

$I_0$  is the reverse saturation or the leakage current of the diode. The leakage current in parallel resistance is given by

$$I_p = \frac{V_{pv} + R_s \cdot I_{pv}}{R_p} \quad (4)$$

where  $V_{pv}$  is the PV output voltage,  $R_s$  is the series resistance, and  $R_p$  is the parallel resistance. Finally, the output current of the PV cell can be obtained as follows:

$$I_{pv} = \left( \frac{G}{G_{ref}} \right) \cdot (I_{ph,ref} + \mu_{sc} \cdot \Delta T) - I_0 \left[ \exp \left( \frac{V_{pv} + R_s \cdot I_{pv}}{A \cdot N_s \cdot V_t} \right) - 1 \right] - \frac{V_{pv} + R_s \cdot I_{pv}}{R_p} \quad (5)$$

where  $N_s$  is the number of series PV cells,  $A$  is the ideality factor, and  $V_t$  is the thermal voltage.

The photovoltaic (PV) array in this study comprises two parallel strings. Each string consists of a series connection of nine PV modules. Figure 3 presents the P-V and I-V characteristics of the photovoltaic (PV) system investigated in this research, considering various climatic circumstances. It is evident that in order to achieve the maximum power point (MPP), it is necessary to adjust the photovoltaic (PV) terminal voltage to  $V_{mpp}$ , which represents the voltage at the maximum power point [30]. This paper presents a photovoltaic (PV) system consisting of a specific PV module, namely, the Sun Power SPR-305-WHT. Therefore, it is obvious from Figure 3a,b that show the I-V and P-V characteristics respectively, the maximum power extracted under standard test conditions (STCs) is about 5.5 kW.

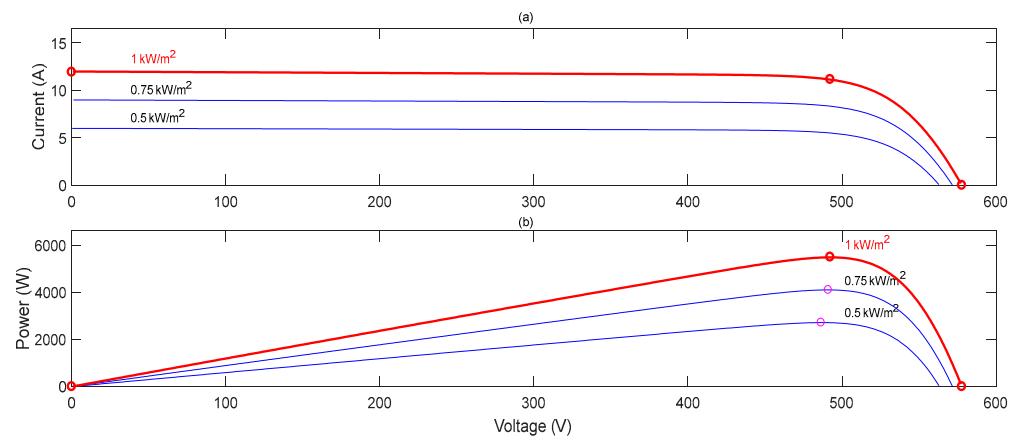


**Figure 3.** P–V (b) and I–V (a) characteristics of the PV array used.

### 2.1.2. Wind Energy Conversion System Modeling

In the field of wind energy conversion systems, various topologies are available for implementation, contingent upon the specific type of generator employed [31,32]. In the current study, the selection of a wind turbine utilizing a permanent magnet synchronous generator (PMSG) and a switching mode rectifier, which is coupled with a DC/DC boost converter, is justified based on its primary intrinsic attributes [31]:

- The self-excitation of the PMSG;
- The output voltage of the boost converter can be adjusted to fit the requirements of the inverter;
- The control simplicity;
- The reduced cost.

### Wind Turbine Modeling

According to [33], the mechanical power acquired by a wind turbine can be accurately described using the following mathematical expression:

$$P_m = \frac{1}{2} \rho A V_w^3 C_p(\lambda, \beta) \quad (6)$$

where  $\rho$  is the air density,  $A$  is the swept area covered by the blades,  $V_w$  is the wind speed,  $C_p$  is the power coefficient.  $\lambda$  is the tip speed ratio.  $\beta$  is the pitch angle, and  $C_p(\lambda, \beta)$  is a nonlinear function related to tip speed ratio ( $\lambda$ ) and the blade pitch angle ( $\beta$ ) which can be described as follows [33]:

$$C_p(\lambda, \beta) = 0.5176\beta \left( 116 \times \frac{1}{\lambda_i} - 0.4\beta - 5 \right) e^{\frac{-21}{\lambda_i}} + 0.0068\lambda \quad (7)$$

$$\frac{1}{\lambda_i} = \frac{1}{(\lambda + 0.08\beta)} - \frac{0.035}{1 + \beta^3} \quad (8)$$

$$\lambda = \frac{R\omega_m}{V_w} \quad (9)$$

where  $R$  is the radius of the turbine and  $\omega_m$  is the rotor speed. The mechanical torque is defined as follows:

$$T_m = \frac{P_m}{\omega_m} = \frac{\frac{1}{2} \rho A V_w^3 C_p(\lambda, \beta)}{\omega_m} \quad (10)$$

It is evident from Equation (7) that with a constant pitch angle  $\beta$ , there is an optimum rotor speed that corresponds to achieving maximum power for each wind speed. Figure 4 shows the characteristics of a wind turbine developed at  $\beta = 0^\circ$  for different wind speeds.

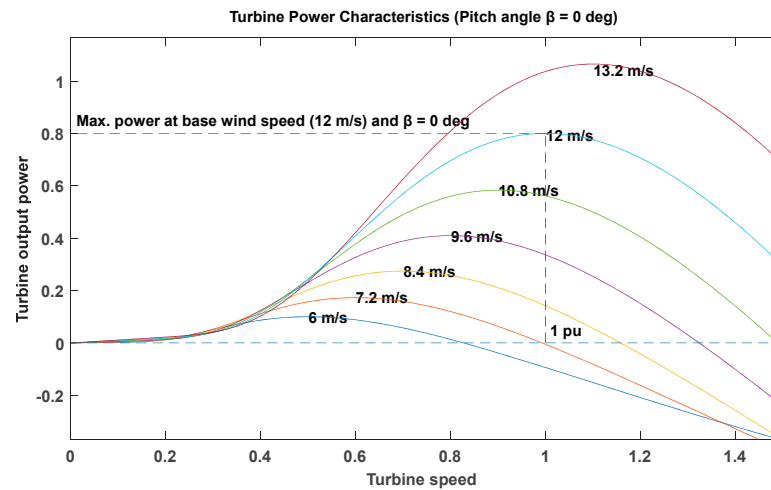


**Figure 4.** Wind turbine power characteristics.

Figure 4 illustrates the ideal correlation between the turbine's output power and speed. The provided diagram depicts the process of optimizing the extraction of power from varying wind speeds to attain the optimum power potential. The power generator within the wind turbine operates through the utilization of a permanent magnet synchronous generator (PMSG). It is worth noting that the power coefficient (CP) of the turbine rotor reaches its maximum value when the blade pitch angle ( $\beta$ ) is set to zero. The wind turbine initially generates mechanical torque per unit, which is then converted into effective torque by multiplying it with the base torque. The aforementioned torque is ultimately exerted on the shaft of the permanent magnet synchronous generator (PMSG). The highest level of power generated, attained when the wind speed is at its base value of 12 m per second, aligns with the nominal speed of the generator set at 1 per unit [34].

#### PMSG Modeling

The stator voltage of the PMSG can be written in a d-q reference frame as follows [35]:

$$V_d = R_S i_d + L_d \frac{di_d}{dt} - L_q i_q \omega_e \quad (11)$$

$$V_q = R_S i_q + L_q \frac{di_q}{dt} + \omega_e (L_d i_d + \varphi) \quad (12)$$

where  $\varphi$  is the permanent magnet's leakage flux (Wb),  $R_S$  is the stator phase resistance ( $\Omega$ ),  $i_d$  and  $i_q$  are the d-q axes stator currents, and ( $L_d = L_q$ ) are the d-q axes inductances in H; they are equal due to the fact that the PMSG considered herein has a salient rotor with  $\omega_e$  is the electrical speed, which is expressed as

$$\omega_e = p \omega_m \quad (13)$$

where  $p$  is the number of pole pairs and  $p \omega_m$  is the mechanical speed.

The mechanical equation of the WECS can be represented as follows [36]:

$$J \frac{d\omega_m}{dt} = T_m - T_e - f \omega_m \quad (14)$$

$$T_e = \frac{3}{2} p i_q \varphi \quad (15)$$

Since there is no gear box between the turbine and the generator,  $J$  is the total inertia of the system (turbine and generator),  $f$  is the viscous friction coefficient,  $T_m$  is the mechanical torque, and  $T_e$  is the electromagnetic torque.

### 3. The Proposed Control Scheme

This section presents design details of the proposed control approach, which operates in the two aforementioned operating modes.

#### 3.1. Operatinh Mode 1: Power Injection Operating Mode

##### 3.1.1. The d-q Reference Current Identification

This strategy is based on a synchronous rotating reference frame (d-q control), which is divided into outer and inner loop controls. The outer voltage loop is used to stabilize or manage the DC-link voltage ( $V_{dc}$ ) by comparing the measured value of the DC-link voltage with the reference value via a PI regulator. The inner loop uses the Park transformation, in which the source currents are transformed into d-q components and then compared with their d-q reference components. The d-axis current reference component presents the output of the outer loop, and the q-axis reference current component is chosen to be equal to zero to ensure the operating mode at the unity power factor [37,38].

##### 3.1.2. Hysteresis Current Control

The hysteresis current controller is one of the most frequently used controllers in AC power systems since it is easy to implement without knowing the system parameters. This technique operates via a comparison of the actual grid currents and their references  $i_{ref}$  with fixed bands. The output of the VSI is switched to low when the generated error is greater than the upper band, and it is switched to high when the error is less than the lower band [39], as shown in Figure 5.

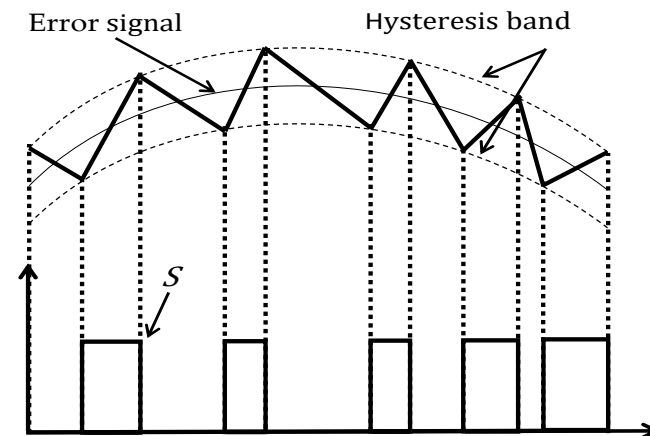


Figure 5. Hysteresis control strategy.

Therefore, to achieve the desired output waveform, the hysteresis band (HB) must be chosen well. The control scheme of this strategy is illustrated in Figure 5.

##### 3.1.3. Backstepping Current Control

To achieve higher levels of stability and performance for the studied grid-tied hybrid system, which is considered a nonlinear system, backstepping control (BSC) approaches are applied due to their advantages over the other nonlinear control methods in terms of systematic and iterative design processes [40,41]. Indeed, the backstepping technique is based on the stabilization of virtual command inputs for first-order subsystems through Lyapunov functions in order to ensure that the system converges to the equilibrium point [42].

Model of the grid voltages in the d-q frame are represented as follows:

$$\begin{aligned} V_{sd} &= V_{id} - R_s \cdot i_{sd} - L_s \cdot \frac{d(i_{sd})}{dt} + \omega_g \cdot (L_s \cdot i_{sq}) \\ V_{sq} &= V_{iq} - R_s \cdot i_{sq} - L_s \cdot \frac{d(i_{sq})}{dt} - \omega_g \cdot (L_s \cdot i_{sd}) \end{aligned} \quad (16)$$

where  $R_s$  and  $L_s$  present the resistance and the inductance of the filter output filter, respectively, and  $\omega_g$  is the angular pulsation of the grid.

The following equation illustrates the dynamics of the currents injected into the grid:

$$\begin{aligned}\frac{d(i_{sd})}{dt} &= \frac{V_{id}}{L_s} - \frac{R_s}{L_s} \cdot i_{sd} + \omega_g \cdot i_{sq} - \frac{V_{sd}}{L_s} \\ \frac{d(i_{sd})}{dt} &= \frac{V_{id}}{L_s} - \frac{R_s}{L_s} \cdot i_{sd} + \omega_g \cdot i_{sq} - \frac{V_{sd}}{L_s} \\ \frac{d(i_{sq})}{dt} &= \frac{V_{iq}}{L_s} - \frac{R_s}{L_s} \cdot i_{sq} - \omega_g \cdot i_{sd} - \frac{V_{sq}}{L_s}\end{aligned}\quad (17)$$

where  $V_{sd}$  and  $V_{sq}$  are the inputs and  $i_{sd}$  and  $i_{sq}$  are the outputs.

The backstepping control was designed based on the following steps.

In the first step, the current errors between the actual current and the reference currents following the d-q frame are defined as follows:

$$\begin{aligned}e_d &= i_{sd\_ref} - i_{sd} \\ e_q &= i_{sq\_ref} - i_{sq}\end{aligned}\quad (18)$$

In order to operate with a unit power factor, the reactive has to be set to zero, which means that the reference current along the q-axis is equal to zero ( $i_{sq\_ref} = 0$ ). On the other side, the reference current  $i_{sd\_ref}$  is obtained through the output of the PI controller of the DC bus voltage. It is obvious that the main aim is to keep these two errors convergent to zero.

In the second step, the derivatives of the current errors are obtained as follows:

$$\begin{aligned}\dot{e}_d &= \dot{i}_{sd\_ref} - \dot{i}_{sd} \\ \dot{e}_q &= \dot{i}_{sq\_ref} - \dot{i}_{sq}\end{aligned}\quad (19)$$

Based on Equation (17), Equation (19) can be rewritten as follows:

$$\begin{aligned}\dot{e}_d &= \dot{i}_{sd\_ref} - \frac{d(i_{sd})}{dt} = \frac{V_{id}}{L_s} - \frac{R_s}{L_s} \cdot i_{sd} + \omega_g \cdot i_{sq} - \frac{V_{sd}}{L_s} \\ \dot{e}_q &= \dot{i}_{sq\_ref} - \frac{d(i_{sq})}{dt} = \frac{V_{iq}}{L_s} - \frac{R_s}{L_s} \cdot i_{sq} - \omega_g \cdot i_{sd} - \frac{V_{sq}}{L_s}\end{aligned}\quad (20)$$

In the third step, a candidate of the Lyapunov function is chosen, and its derivative is calculated as follows:

$$\begin{cases} V_1 = \frac{1}{2}(e_d^2 + e_q^2) \\ \dot{V}_1 = e_d \cdot \dot{e}_d + e_q \cdot \dot{e}_q \end{cases}\quad (21)$$

The main objective is to ensure that the two errors converge to zero and the system's stability is maintained. Indeed, based on the Lyapunov theorem, these conditions can be met if the derivative of the proposed Lyapunov function is strictly negative, meaning that  $\dot{V}_1 < 0$ ,  $\dot{V}_2 < 0$ . In this context, the derivatives of the aforementioned error functions are presented as follows:

$$\begin{aligned}\dot{e}_d &= -K_d e_d \\ \dot{e}_q &= -K_q e_q\end{aligned}\quad (22)$$

According to the condition of Lyapunov, the two constants  $K_d$  and  $K_q$  must be positive. From (20) and (22), the following equations are obtained:

$$\begin{aligned}\frac{V_{id}}{L_s} - \frac{R_s}{L_s} \cdot i_{sd} + \omega_g \cdot i_{sq} - \frac{V_{sd}}{L_s} &= -K_d e_d \\ \frac{V_{iq}}{L_s} - \frac{R_s}{L_s} \cdot i_{sq} - \omega_g \cdot i_{sd} - \frac{V_{sq}}{L_s} &= -K_q e_q\end{aligned}\quad (23)$$

Consequently, the reference voltages will be

$$\begin{cases} V_{id\_ref} = R_s \cdot i_{sd} - L_s \cdot \omega_g \cdot i_{sq} - L_s \cdot K_d \cdot e_d + V_{sd} \\ V_{iq\_ref} = R_s \cdot i_{sq} + L_s \cdot \omega_g \cdot i_{sd} - L_s \cdot K_q \cdot e_q + V_{sq} \end{cases}\quad (24)$$

### 3.2. Operating Mode 2: Power Quality Improvement Operating Mode

#### 3.2.1. Reference Current Identification

In order to accurately mitigate the circulation of the current harmonics toward the power source via the suggested SAPF architecture, it is imperative to accurately identify the current harmonics. Indeed, numerous methodologies have been put forth in a multitude of prior studies. In this particular research study, synchronous reference frame methodology is employed owing to its uncomplicated design and accurate functionality [21–24]. The underlying premise of this system relies on the conversion of load currents from the natural frame (abc) to their corresponding dq components in the dq frame [43,44]. In this frame, the q-axis is aligned with the  $\alpha$ -axis at  $t = 0$ . The schematic representation of the synchronous reference frame method is shown in Figure 6. In this strategy, the three-phase instantaneous load currents are first transformed into  $\alpha$ - $\beta$  coordinates using the Clarke transformation. Subsequently, these coordinates are further converted into the d-q frame using the Park transformation, according to the following procedure:

$$\begin{bmatrix} il_{\alpha} \\ il_{\beta} \end{bmatrix} = \frac{2}{3} \begin{bmatrix} 1 & -\frac{1}{2} & -\frac{1}{2} \\ 0 & \frac{\sqrt{3}}{2} & -\frac{\sqrt{3}}{2} \end{bmatrix} \begin{bmatrix} il_a \\ il_b \\ il_c \end{bmatrix} \tag{25}$$

$$\begin{bmatrix} il_d \\ il_q \end{bmatrix} = \begin{bmatrix} \sin(\theta) & -\cos(\theta) \\ \cos(\theta) & \sin(\theta) \end{bmatrix} \begin{bmatrix} il_{\alpha} \\ il_{\beta} \end{bmatrix} \tag{26}$$

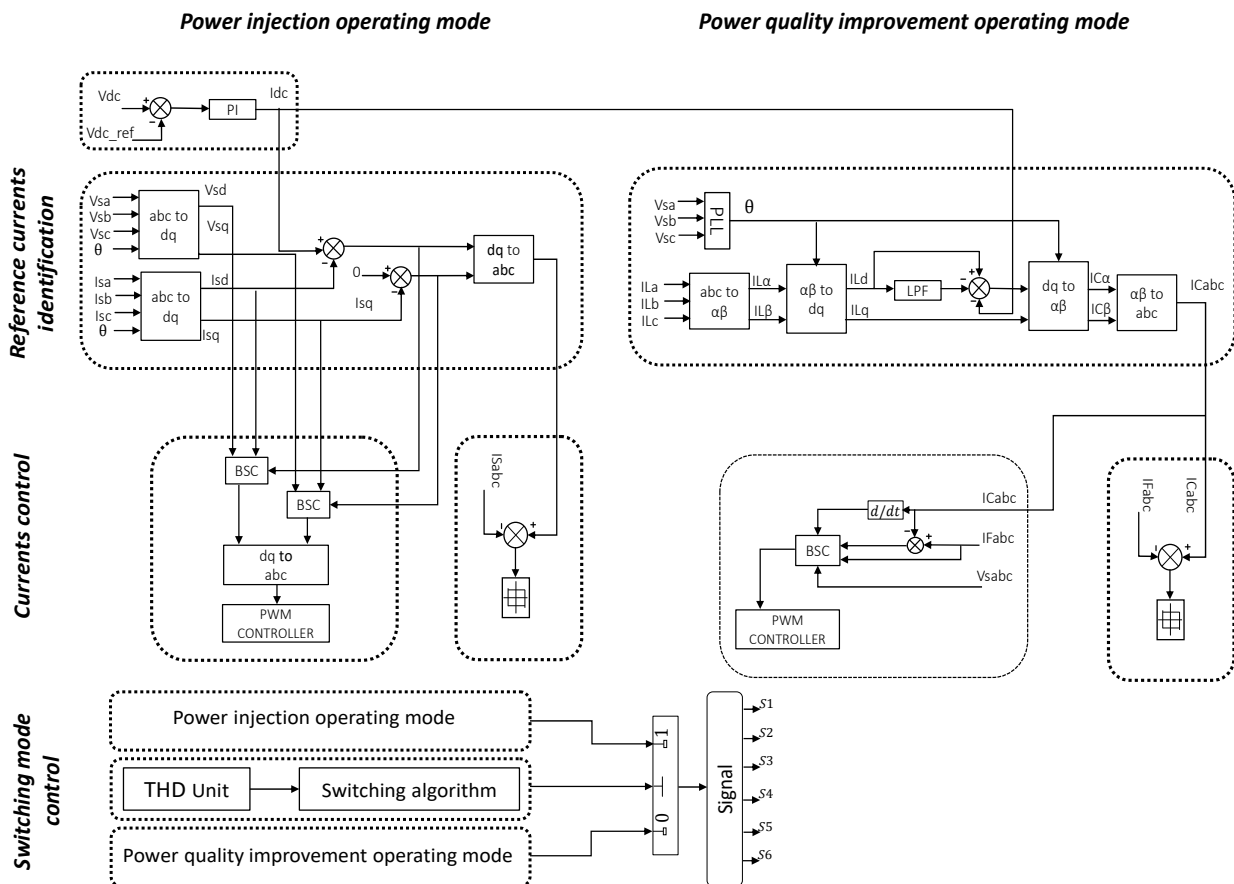


Figure 6. Flowchart of the control system.

The synchronization angle  $\theta$  is obtained using a PLL unit, as shown in Figure 6.

Each of the obtained d-q load currents are further decomposed to a DC component and an oscillatory component using a low-pass filter (LPF) with a cutting frequency of 50 Hz, as shown in Figure 6. Hence, the load current can be written as follows:

$$\begin{bmatrix} iC_d \\ iC_q \end{bmatrix} = \begin{bmatrix} \bar{i}l_d + \tilde{i}l_d \\ \bar{i}l_q + \tilde{i}l_q \end{bmatrix} \quad (27)$$

The output of the DC bus controller should be added; it represents the losses in the VSI and should therefore be considered within the d components. Furthermore, to ensure the reactive components of the current are compensated, the DC component within the  $q$ -axis should be added. Finally, the compensating current generated by the VSI and injected into the PCC following the  $\alpha$ - $\beta$  frame can be obtained as follows:

$$\begin{bmatrix} ic_\alpha \\ ic_\beta \end{bmatrix} = \begin{bmatrix} \sin(\theta) & \cos(\theta) \\ -\cos(\theta) & \sin(\theta) \end{bmatrix} \begin{bmatrix} \bar{i}l_d - i_{dc} \\ \bar{i}l_q + \tilde{i}l_q \end{bmatrix} \quad (28)$$

Using the inverse Park transformation, the desired reference current that should be injected to the PCC can be obtained as follows:

$$\begin{bmatrix} ic_a \\ ic_b \\ ic_c \end{bmatrix} = \begin{bmatrix} 1 & 0 \\ -\frac{1}{2} & \frac{\sqrt{3}}{2} \\ -\frac{1}{2} & -\frac{\sqrt{3}}{2} \end{bmatrix} \begin{bmatrix} ic_\alpha \\ ic_\beta \end{bmatrix} \quad (29)$$

### 3.2.2. Hysteresis Current Control

As described in Section 3.1.1, the reference current generated by the SRF theory depends upon the expression of the switching pulses generated [45], whose operating functions are defined as follows:

The upper switch is ON and the lower switch is OFF when

$$I_c - I_c < HB$$

The upper switch is OFF and the lower switch is ON when

$$I_c - I_c > HB$$

### 3.2.3. Backstepping Controller

The current control scheme based on a backstepping controller is shown in Figure 6; it was inspired by the study described in [13]. The current errors and their derivatives in the natural frame ( $abc$ ) can be described as follows:

$$\begin{cases} e_1 = if_a - ic_a \\ e_2 = if_b - ic_b \\ e_3 = if_c - ic_c \end{cases} \quad (30)$$

Their derivatives are given by

$$\begin{cases} \dot{e}_1 = \dot{if}_a - \dot{ic}_a \\ \dot{e}_2 = \dot{if}_b - \dot{ic}_b \\ \dot{e}_3 = \dot{if}_c - \dot{ic}_c \end{cases} \quad (31)$$

The proposed Lyapunov function is

$$V = V_1 + V_2 + V_3 \quad (32)$$

where

$$\begin{cases} V_1 = \frac{1}{2}e_1^2 \\ V_2 = \frac{1}{2}e_2^2 \\ V_3 = \frac{1}{2}e_3^2 \end{cases} \quad (33)$$

The derivatives of the Lyapunov function's components can be represented by

$$\begin{aligned} \dot{V}_1 &= e_1 \dot{e}_1 = e_1 \left( \frac{1}{L_{fa}} (v_{fa} - v_{sa} - R_{fa} i_{fa}) - \dot{i}_a \right) \\ \dot{V}_2 &= e_2 \dot{e}_2 = e_2 \left( \frac{1}{L_{fb}} (v_{fb} - v_{sb} - R_{fb} i_{fb}) - \dot{i}_b \right) \\ \dot{V}_3 &= e_3 \dot{e}_3 = e_3 \left( \frac{1}{L_{fc}} (v_{fc} - v_{sc} - R_{fc} i_{fc}) - \dot{i}_c \right) \end{aligned} \quad (34)$$

Finally, the reference output voltages of the APF can be obtained as follows:

$$\begin{cases} V_{faref} = L_{fa} (\dot{i}_a - Ke_1) + v_{sa} + R_{fa} i_{fa} \\ V_{fbref} = L_{fb} (\dot{i}_b - Ke_2) + v_{sb} + R_{fb} i_{fb} \\ V_{fcref} = L_{fc} (\dot{i}_c - Ke_3) + v_{sc} + R_{fc} i_{fc} \end{cases} \quad (35)$$

#### 4. Simulation Results

For the examination of the effectiveness of the multifunctional control technique proposed in this paper, simulation tests of the system presented in Figure 1 were carried out via MATLAB/SIMULINK for the aforementioned modes. To assess the robustness of the proposed system, it was tested for the two aforementioned operating modes such that during operating mode 1, the hybrid energy sources were exposed to various climatic conditions such as variable wind and irradiance profiles, as shown in Figure 7. Furthermore, in operating mode 2, a sudden degradation of the current quality of the main grid occurred due to the connection of non-linear loads.

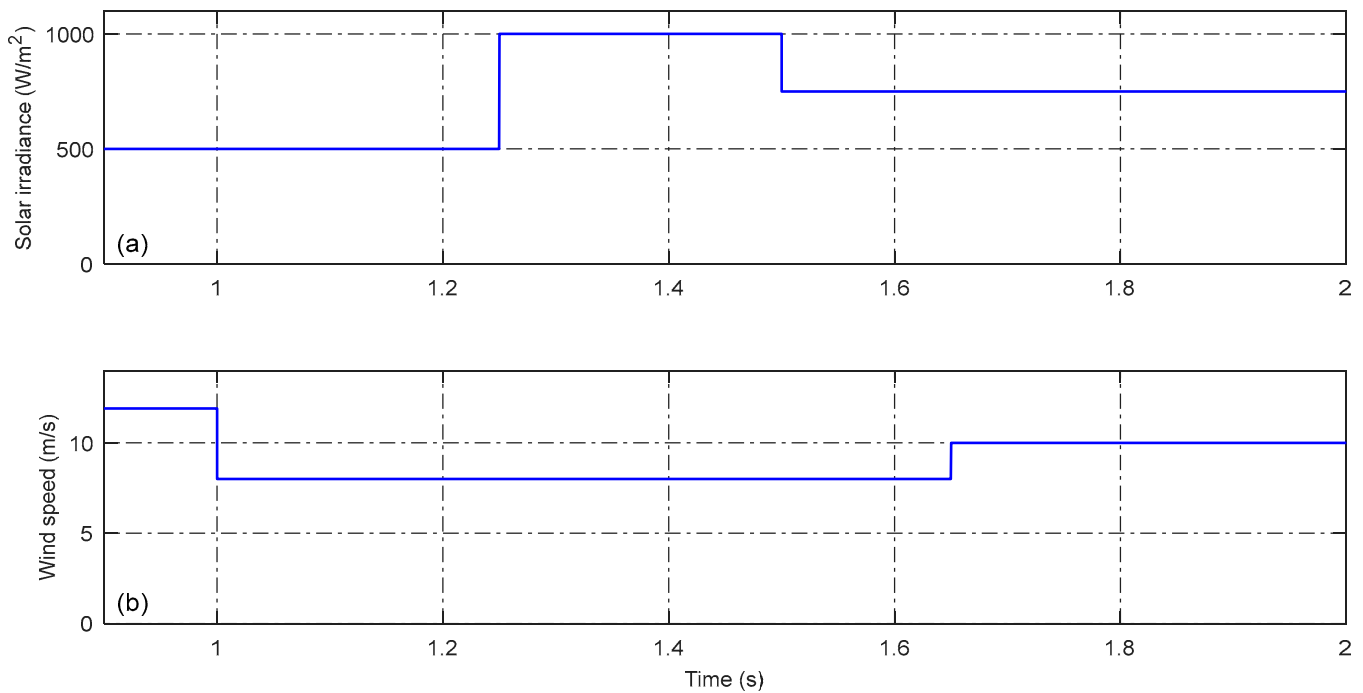


Figure 7. (a) Irradiance profile; (b) wind speed profile.

The selection of the values of the parameters of the proposed system were made based on [24], and they are presented in Table 1.

**Table 1.** Parameter values.

	Parameters	Value
	Grid voltage (Vs)	400 V
	System frequency (f)	50 Hz
	Supply inductance	20 $\mu$ H
	Supply resistance	0.3 $\Omega$
	DC link capacitor	5000 $\mu$ F
Wind system	Maximum wind power	6 kW
	PMSG stator phase resistance (Rs)	0.425 $\Omega$
	PMSG armature inductance Ld = Lq	$8.4 \times 10^{-3}$ H;
	Leakage flux	0.433 Wb
	No. of poles	5
PV system	Maximum PV power	5.5 kW
	No. of series cells Ns	9
	No. of parallel cells Np	2

*4.1. Operating Mode 1: Power Injection Mode*

Figure 8 illustrates the power produced from the PV source and the wind source for both of the current controllers used: the hysteresis controller and the backstepping controller. In this operating mode, the incremental inductance MPPT algorithm is utilized to control the boost converters for the two systems, boost converter I and boost converter II, as shown in Figure 1. Indeed, the maximum extracted power values for both sources, which were obtained based on the MPPT algorithm used under variable climatic conditions, are shown in Figure 7a,b. Figure 8a illustrates the power produced from the PV source at different irradiation values. It can be clearly seen that starting from 2 s, the irradiation increased suddenly from 500 to 1000 W/m<sup>2</sup> and then decreased to 750 W/m<sup>2</sup> at 2.5 s. Figure 8b presents the wind power with varying wind speeds. The InC algorithm introduced a quick response and tracked the maximum power point despite the instantaneous change in irradiance and the wind speed’s drop and rise, with slight advantages in the case of backstepping current control, as shown in the zoom boxes.

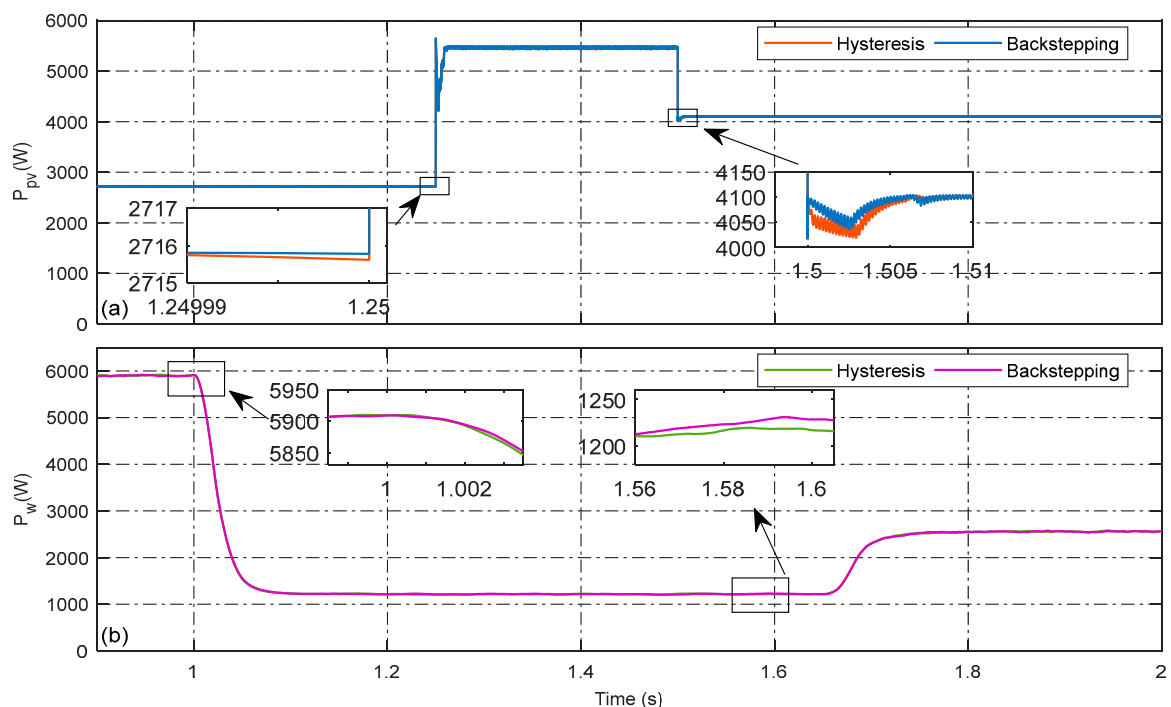


**Figure 8.** (a) PV power; (b) wind power.

One of the performance evaluation criteria for a renewable energy hybrid power system is the DC link voltage. In this context, Figure 9a displays the dynamics of the responses of the DC link voltage under different climate variations. It can be observed clearly that the DC link voltage follows the constant reference value, especially in transient steps along the period test. This test proves that despite the changes in the irradiance or wind speed, the DC link voltage is successfully kept quasi-constant and follows its reference value (750 V) with insignificant ripples.

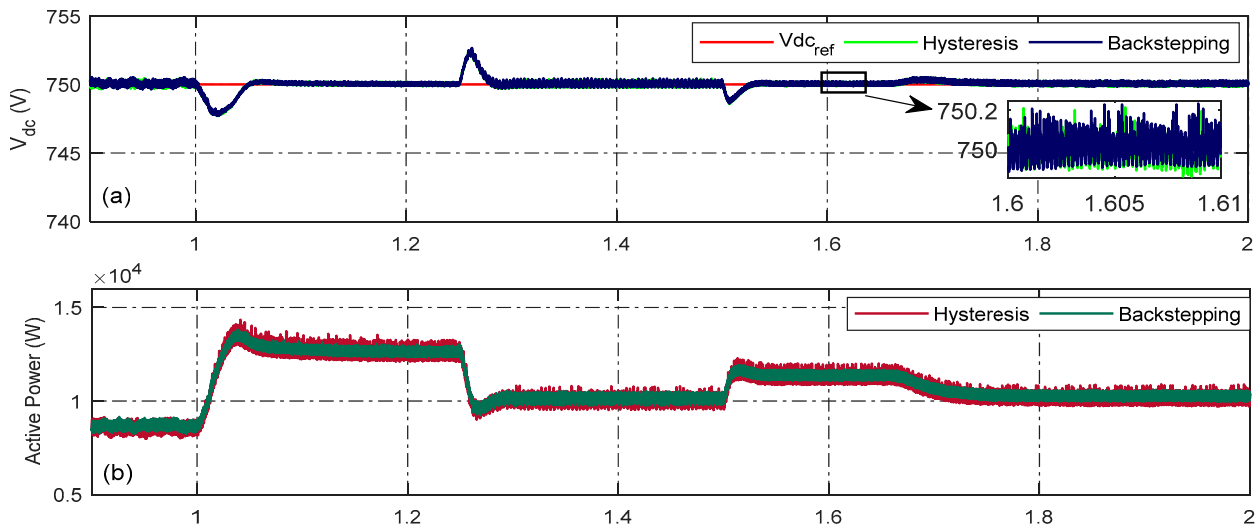


Figure 9. (a) DC link voltage; (b) instantaneous active power.

There is no effect in terms of overshoot for either of the current controls, proving the effectiveness of the adopted control. Figure 9b displays the instantaneous active power produced by the utility grid, which was increased and decreased smoothly due to the power injected by the PV-Wind system, with fewer oscillations observed in the case of the backstepping current control.

Figure 10 illustrates the source current, which has a sine waveform whose magnitudes vary according to the profile of the main climate parameters, such as the irradiance and wind speed. Figure 11 presents the currents injected into the grid at the point of common connection. It can be seen that these currents remain sinusoidal, with amplitudes that vary according to climatic variations, and their frequency is adequate for the grid (50 Hz). Moreover, in the zoomed-in parts, it is apparent that the grid voltage and the injected currents are in phase. Figure 12 illustrates the evaluation of the THD level of the injected current due to hysteresis and backstepping current control. It is obvious that the backstepping controller provides a better injected current THD, which demonstrates the quality of the power fed to the grid.

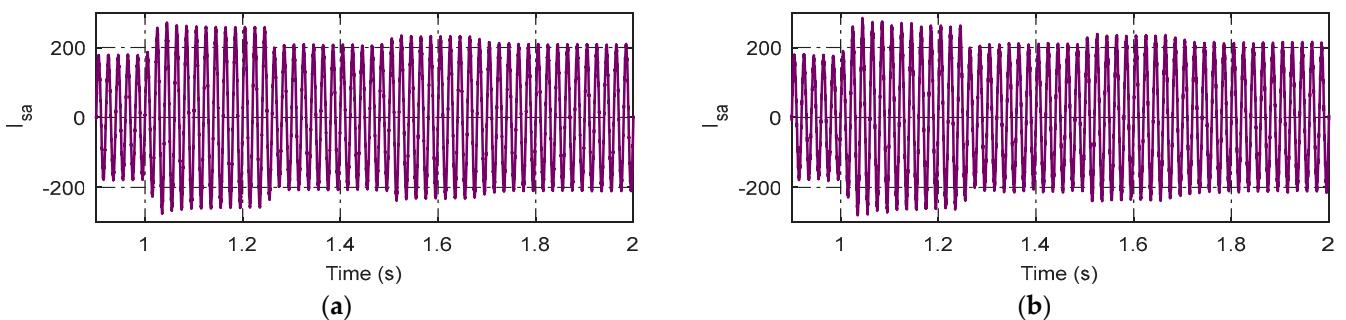


Figure 10. Source current. (a) Backstepping control; (b) hysteresis control.

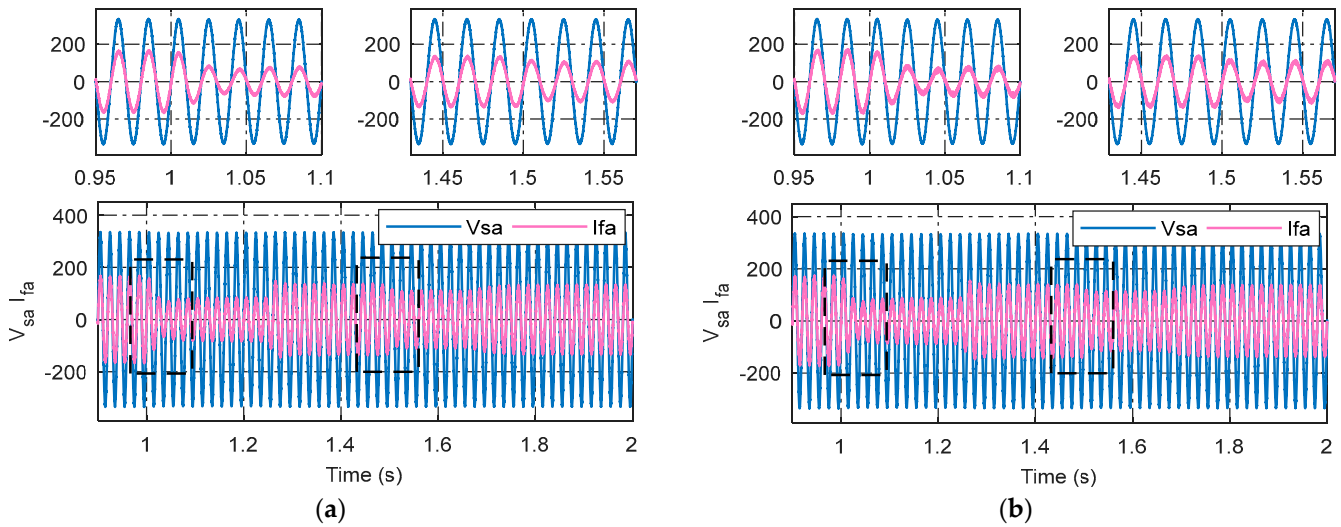


Figure 11. Injected current and voltage. (a) Backstepping control; (b) hysteresis control.

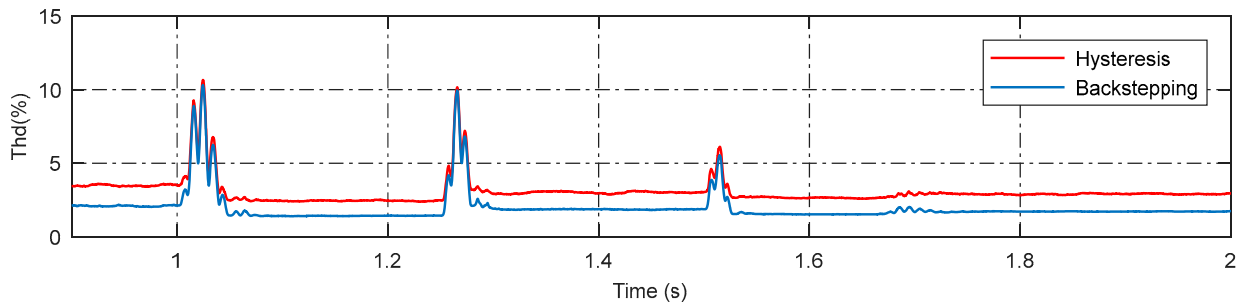


Figure 12. The THD Of the injected current.

4.2. Operating Mode 2: Power Quality Improvement Mode

To test the ability of the proposed multifunctional control technique in operating mode 2 to overcome the main problem of power quality resulting from the power system’s source current due to the connection of a nonlinear load, such as an uncontrolled three-phase diode rectifier that is connected within a period of 0.8 s to 0.93 s, as shown in Figure 13a, Figure 13b shows how the injected current changes its form from purely sinusoidal to compensating currents to satisfy the new criteria and ensure the filtering process after a short transient period. Figure 13c shows that the source current is decontaminated with slight peaks at the instances of the nonlinear load connections. Figure 14 displays the load current, injected current, and source current under hysteresis current control, wherein significant peaks are introduced at switching instants compared to the backstepping controller.

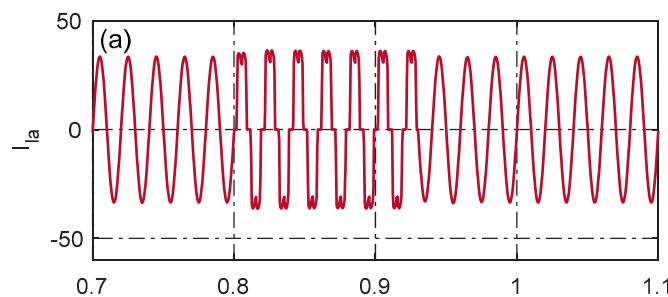


Figure 13. Cont.

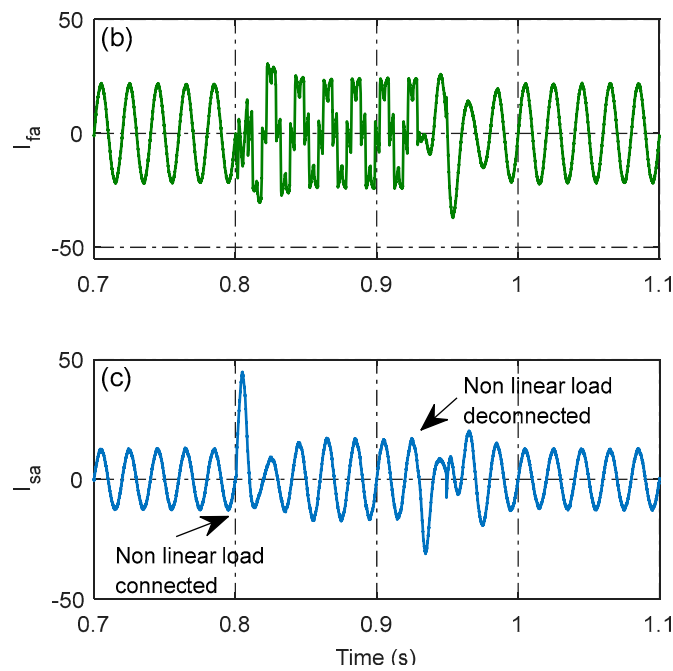


Figure 13. Backstepping current control: (a) load current; (b) injected current; (c) source current.

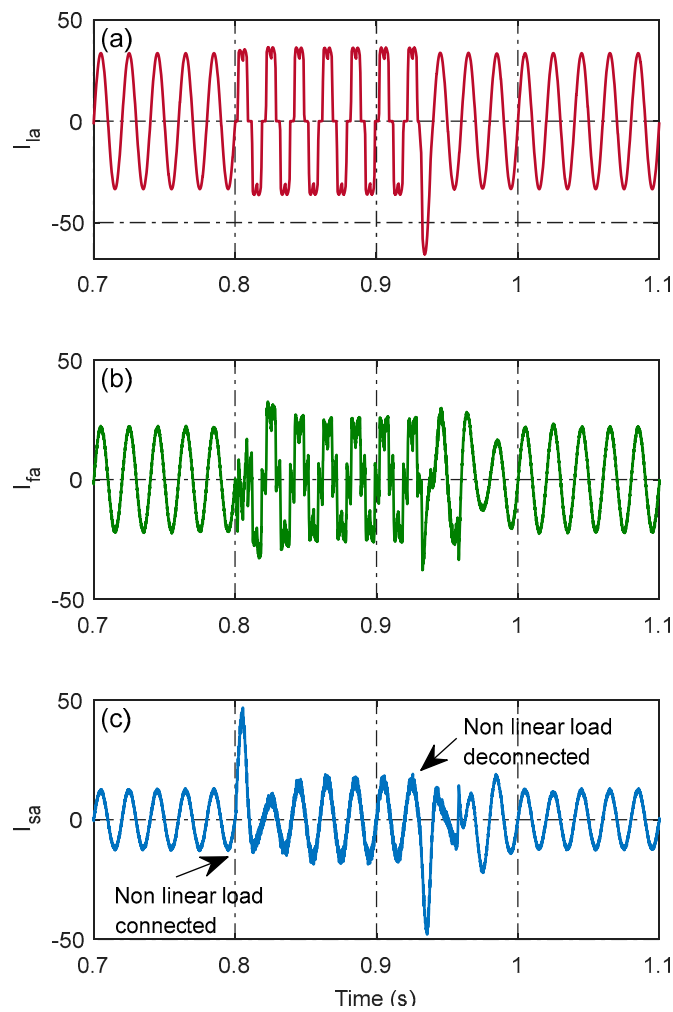


Figure 14. Hysteresis current control: (a) load current; (b) injected current; (c) source current.

Figure 15a shows the dynamic behavior of the DC-link under both current control strategies. It is obvious that small deviations occur at the moments at which the nonlinear load is connected and disconnected. However, the backstepping controller has a low peak and short transient recovery times compared to the hysteresis controller. Meanwhile, the proposed control provides good reactive power compensation that oscillates around zero, as shown in Figure 15b, where it can be observed that the backstepping has ensured fewer ripples.

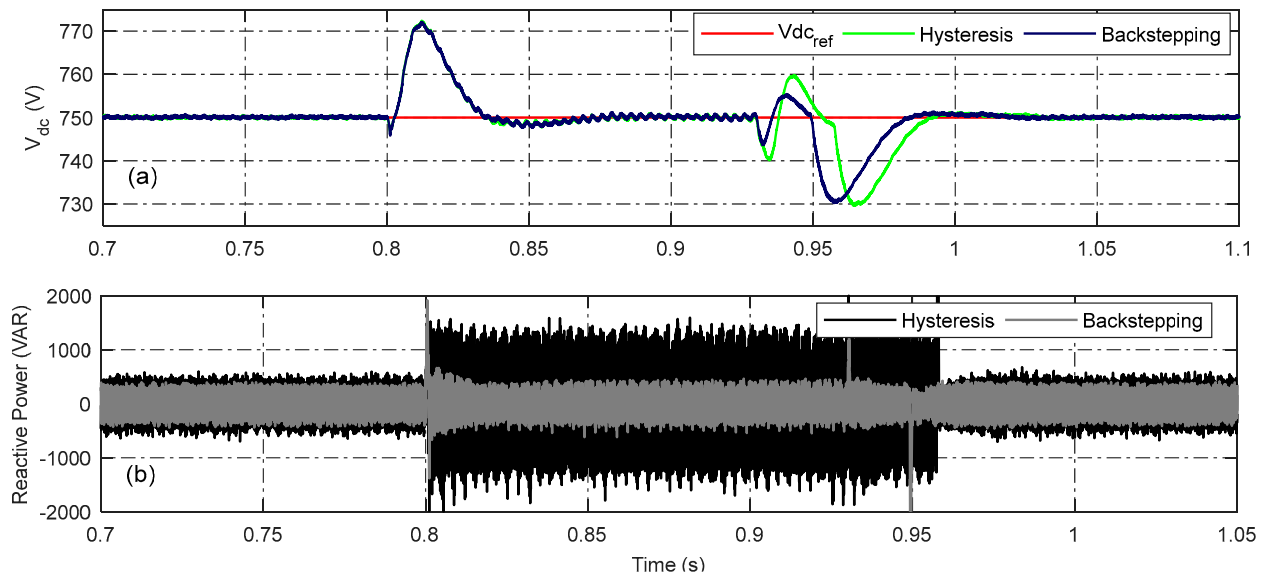


Figure 15. (a) DC link voltage; (b) reactive power.

Figure 16 shows the source current's THD. It can be noted that significant increases in the THD occurred at 0.8 s and 0.93 s due to the connection and disconnection of the nonlinear load. Overall, it can be seen that in the case of backstepping, the THD is less than 5%, which meets the IEEE 519 harmonics standards, unlike when the hysteresis controller is used, wherein the source current is distorted and the THD is high.

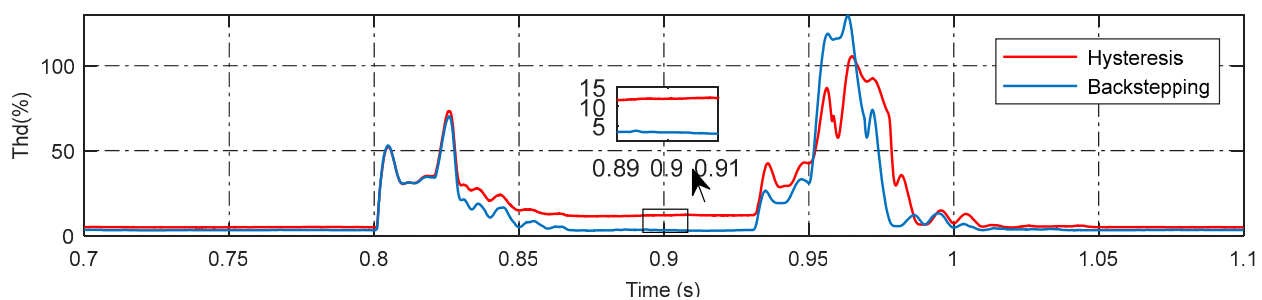
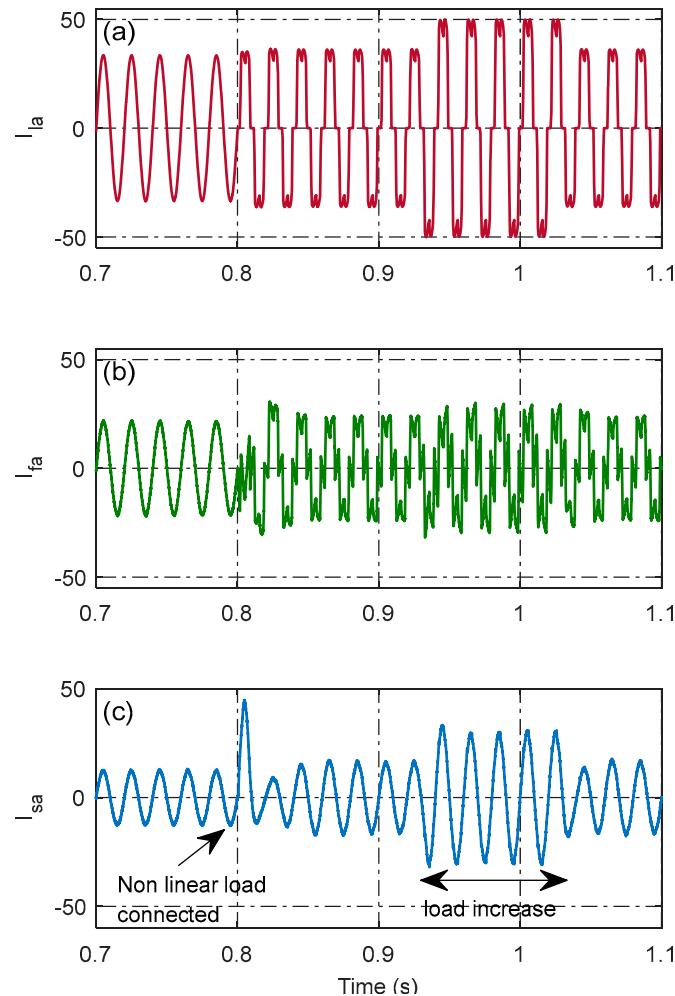


Figure 16. The THD of the source current.

#### 4.3. Dynamic Load Conditions

To ensure the quality performance of the proposed control technique, the studied multi-source power system was tested under dynamic load conditions in which a sudden load demand increase and decrease occurred. As can be observed clearly in Figures 17a and 18a, a nonlinear load was connected at 0.8 s, which was confirmed by the deformation of the load current compared to the initial sine waveform. Then, an increase in the load demand of 35% occurred at 0.93 s, and the load demand was finally decreased to return to its initial value under the connection of the nonlinear load. Figure 17b,c show the dynamic behavior of the injected current and the power system's source current in relation to the behavior of the load variations based on the application of the backstepping controller. Figure 18b,c

show the same behavior dynamic of the injected current and the power source current. It is clear that the injected current is adjusted to fulfill the new load change requirements in order to continue to mitigate the harmonics generated by the nonlinear load and to keep the power system's source current healthy under the sine waveform, where its magnitude changes in accordance with changes in the load, as shown in both figures, respectively. It can be deduced from the obtained power system source currents in Figures 17c and 18c that the backstepping controller ensured fewer ripples in the power system's source current compared to the hysteresis controller.



**Figure 17.** Backstepping current control: (a) load current; (b) injected current; (c) source current.

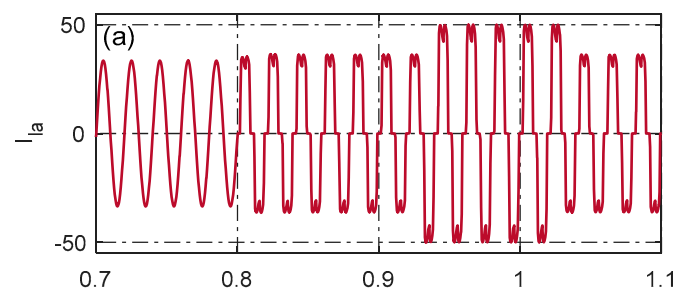


**Figure 18.** Cont.

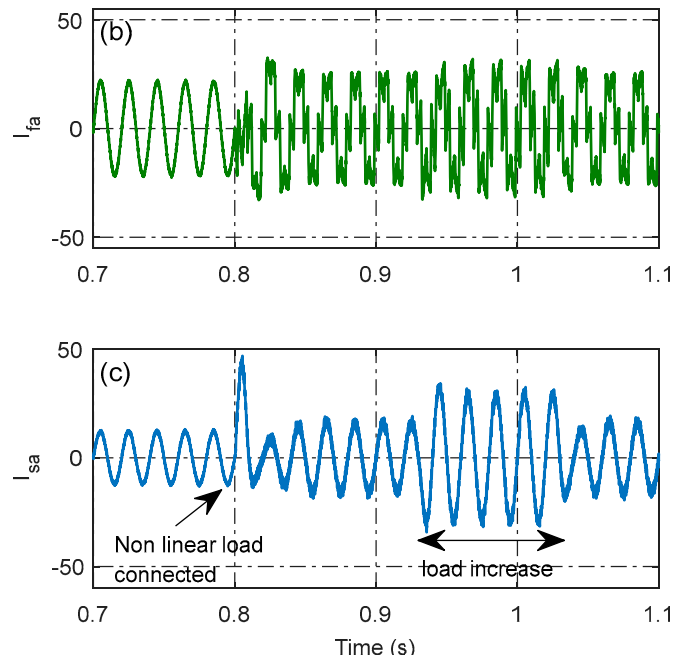


Figure 18. Hysteresis current control: (a) load current; (b) injected current; (c) source current.

Furthermore, it can be noticed that when the load varies, there were limited fluctuations in the voltage across the DC link for a very short time, and the reactive power was maintained compensated, as shown in Figure 19a,b, respectively. It is worth mentioning here that the backstepping controller allowed the researchers to ensure that there were fewer ripples in the injected reactive power compared to the hysteresis controller. Additionally, the measured THD values for both controllers following the variations of the load are shown in Figure 20. Based on this figure, it is obvious that the backstepping controller demonstrates superior harmonic mitigation compared to the hysteresis controller; this can be seen throughout the THD profiles shown in Figure 20, with a better percentage achieved by the backstepping current control.

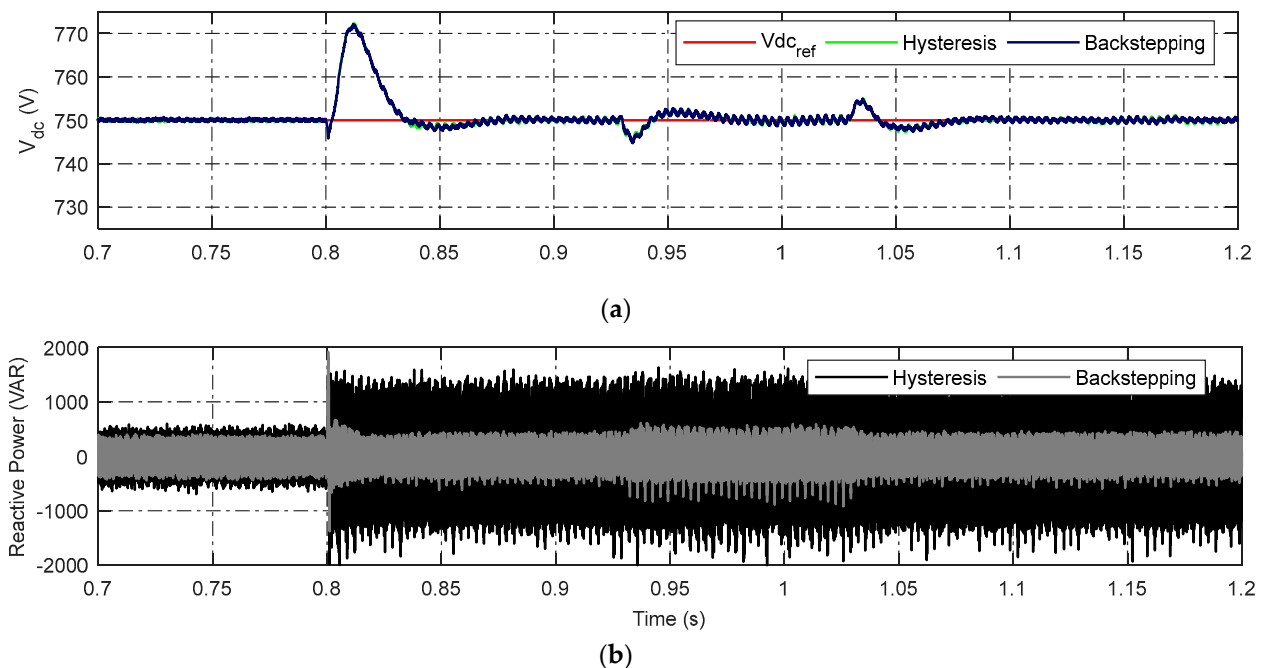
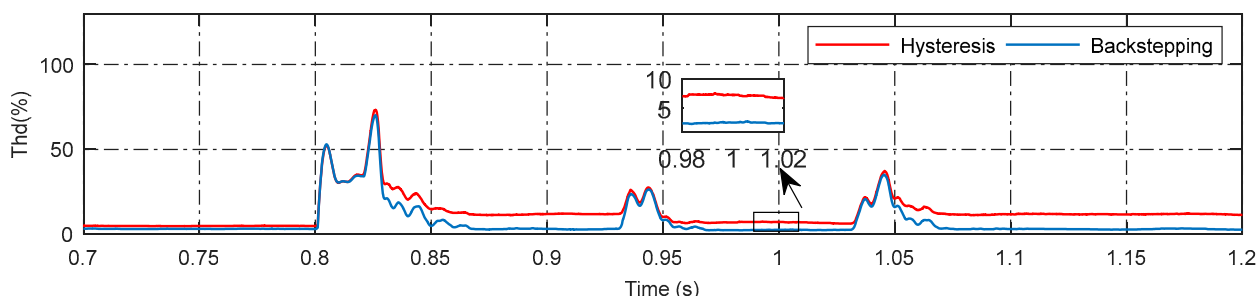


Figure 19. (a) DC link voltage; (b) reactive power.



**Figure 20.** The THD of the source current.

An overall comparison analysis of the two controllers is summarized in Table 2. The proposed system provides good maximum power tracking for the wind and the PV source using both current controllers, with an accuracy of  $>96\%$ . For operating mode 1, the backstepping controller demonstrated superior performance in terms of the quality of the injected current, with a THD of less than 2%, and the stability of the instantaneous active power, which encountered lower oscillations compared to the hysteresis controller. Likewise, for the power quality improvement in operating mode 2, the backstepping controller introduced higher harmonic mitigation that was proven within the measured THD profile of the power system's source current, which remained within the acceptable range over the entire load variation profile. Unlike in the case in which the hysteresis controller was used, the source current was more distorted (THDS  $> 5\%$ ) compared to the obtained THD under the application of the backstepping controller, meaning that the hysteresis controller demonstrated a lesser performance. Furthermore, for the compensation of the reactive power issued from the load and to ensure the power factor of the power system's source was improved, the backstepping controller showed a higher compensation ratio compared to the hysteresis controller. Based on the obtained results for both controllers and both operating modes, it can evidently be said that the backstepping current controller is more efficient in terms of THD reduction, reactive power compensation, and active power stability in both the operating modes investigated, as represented in Table 1, which could make it more suitable solution.

**Table 2.** Overall comparison.

MPPT Efficiency		
PV system		99.45%
Wind system		98.03%
Mode 01: Power injection		
	Backstepping	Hysteresis
THD of source current	1.44%	2.45%
Active power oscillations	low	high
Mode 02: Power improvement		
	Backstepping	Hysteresis
THD of Nonlinear load	3.22%	12%
THD of Dynamic load	2.62%	7.24%
Reactive power compensation	97.14%	84.28%

## 5. Conclusions

This paper presents an extensive investigation into a novel multifunctional control approach applied to a grid-tied hybrid distributed generation system composed of a PV system and a PMSG wind system. The proposed system injects harvested power into the grid and enhances the power quality by reducing the harmful effects of harmonics

produced by non-linear loads connected to the distribution grid. The proposed control scheme includes two modes. Firstly, the system ensures that the power generated from the hybrid system is fed to the utility grid and maintains the unity power factor under unsteady environmental conditions. Secondly, in the case of harmonic contamination appearing in the grid, the proposed system switches to acting as a compensator to eliminate harmonics and compensate for the reactive power. This novel multifunctional control strategy offers several advantages, including the following:

- Enhancing the reliability and efficiency of the power supply by taking advantage of renewable energy sources;
- Mitigating the harmonic current, which eventually decreases the source current's ripples and enhances the overall performance of the grid;
- Providing a smooth, dynamic transition between two modes, which guarantees a consistent input current waveform throughout both modes of operation.

Throughout the presented simulation results, it can be seen that the proposed approach has a superior performance compared to traditional techniques in terms of reducing the THD, reactive power compensation, and the accuracy of tracking the MPP.

**Author Contributions:** Conceptualization, S.A.B., A.M.K., A.K. and A.T.; methodology, S.A.B., A.M.K., A.K., A.B., A.T. and A.H.; software, S.A.B., A.M.K., A.K. and A.T.; validation, S.A.B., A.M.K., A.K. and A.H.; formal analysis, S.A.B., A.M.K., A.K., A.T., M.A. and R.K.; investigation, S.A.B., A.M.K., A.K., A.T., M.A. and R.K.; resources, S.A.B., A.M.K., A.K., A.T., M.A. and R.K.; data accuracy, S.A.B., A.K. and A.T.; writing—original draft preparation, S.A.B., A.K., A.T. and M.A.; writing—review and editing, S.A.B., A.K., A.T., R.K. and M.A.; visualization, S.A.B., A.K. and A.T.; supervision, S.A.B., A.K. and A.T.; project administration, S.A.B., A.K. and A.T. All authors have read and agreed to the published version of the manuscript.

**Funding:** This research received no external funding.

**Data Availability Statement:** Not Applicable.

**Acknowledgments:** This work was supported by the German Research Foundation (DFG) and the Technical University of Munich (TUM) in the framework of the Open Access Publishing Program.

**Conflicts of Interest:** The authors declare no conflict of interest.

## References

1. Cai, T.; Dong, M.; Chen, K.; Gong, T. Methods of participating power spot market bidding and settlement for renewable energy systems. *Energy Rep.* **2022**, *8*, 7764–7772. [[CrossRef](#)]
2. Gajewski, P.; Pieńkowski, K. Control of the Hybrid Renewable Energy System with Wind Turbine, Photovoltaic Panels and Battery Energy Storage. *Energies* **2021**, *14*, 1595. [[CrossRef](#)]
3. Khosravi, N.; Abdolmohammadi, H.R.; Bagheri, S.; Miveh, M.R. A novel control approach for harmonic compensation using switched power filter compensators in micro-grids. *IET Renew. Power Gener.* **2021**, *15*, 3989–4005. [[CrossRef](#)]
4. Rekioua, D. *Hybrid Renewable Energy Systems: Optimization and Power Management Control*; Springer Nature: Berlin, Germany, 2019.
5. Cao, B.; Dong, W.; Lv, Z.; Gu, Y.; Singh, S.; Kumar, P. Hybrid Microgrid Many-Objective Sizing Optimization with Fuzzy Decision. *IEEE Trans. Fuzzy Syst.* **2020**, *28*, 2702–2710. [[CrossRef](#)]
6. Taghieh, A.; Mohammadzadeh, A.; Zhang, C.; Kausar, N.; Castillo, O. A type-3 fuzzy control for current sharing and voltage balancing in microgrids. *Appl. Soft Comput.* **2022**, *129*, 109636. [[CrossRef](#)]
7. Rao, S.N.; Kumar, D.V.A.; Babu, C.S. Grid Connected Distributed Generation System with High Voltage Gain Cascaded DC-DC Converter Fed Asymmetric Multilevel Inverter Topology. *Int. J. Electr. Comput. Eng.* **2018**, *8*, 4047–4059. [[CrossRef](#)]
8. Lin, X.; Wen, Y.; Yu, R.; Yu, J.; Wen, H. Improved Weak Grids Synchronization Unit for Passivity Enhancement of Grid-Connected Inverter. *IEEE J. Emerg. Sel. Top. Power Electron.* **2022**, *10*, 7084–7097. [[CrossRef](#)]
9. Lin, X.; Liu, Y.; Yu, J.; Yu, R.; Zhang, J.; Wen, H. Stability analysis of Three-phase Grid-Connected inverter under the weak grids with asymmetrical grid impedance by LTP theory in time domain. *Int. J. Electr. Power Energy Syst.* **2022**, *142*, 108244. [[CrossRef](#)]
10. Tareen, W.U.K.; Mekhief, S. Three-phase transformerless shunt active power filter with reduced switch count for harmonic compensation in grid-connected applications. *IEEE Trans. Power Electron.* **2017**, *33*, 4868–4881. [[CrossRef](#)]
11. Reddy, C.R.; Goud, B.S.; Aymen, F.; Rao, G.S.; Bortoni, E.C. Power quality improvement in HRES grid connected system with FOPID based atom search optimization technique. *Energies* **2021**, *14*, 5812. [[CrossRef](#)]
12. Liao, K.; Pang, B.; Yang, J.; He, Z. Compensation Strategy of Wideband Voltage Harmonics for Doubly-Fed Induction Generator. *IEEE Trans. Energy Convers.* **2023**, *38*, 674–684. [[CrossRef](#)]

13. Teta, A. Investigation on Active Power Filter Based on Z-Source Inverter Topology. Ph.D. Thesis, Université de Djelfa-Ziane Achour, Djelfa, Algeria, 2021.
14. Liao, K.; Lu, D.; Wang, M.; Yang, J. A Low-Pass Virtual Filter for Output Power Smoothing of Wind Energy Conversion Systems. *IEEE Trans. Ind. Electron.* **2022**, *69*, 12874–12885. [[CrossRef](#)]
15. Rivas, D.; Morán, L.; Dixon, J.W.; Espinoza, J.R. Improving passive filter compensation performance with active techniques. *IEEE Trans. Ind. Electron.* **2003**, *50*, 161–170. [[CrossRef](#)]
16. Lee, T.-L.; Wang, Y.-C.; Li, J.-C.; Guerrero, J.M. Hybrid active filter with variable conductance for harmonic resonance suppression in industrial power systems. *IEEE Trans. Ind. Electron.* **2014**, *62*, 746–756. [[CrossRef](#)]
17. Saidi, S.; Abbassi, R.; Chebbi, S. Quality improvement of shunt active power filter with direct instantaneous power estimator based on Virtual Flux. *Int. J. Control. Autom. Syst.* **2016**, *14*, 1309–1321. [[CrossRef](#)]
18. Pandove, G.; Singh, M. Robust repetitive control design for a three-phase four wire shunt active power filter. *IEEE Trans. Ind. Informatics* **2018**, *15*, 2810–2818. [[CrossRef](#)]
19. Cao, W.; Liu, K.; Wu, M.; Xu, S.; Zhao, J. An improved current control strategy based on particle swarm optimization and steady-state error correction for SAPF. *IEEE Trans. Ind. Appl.* **2019**, *55*, 4268–4274. [[CrossRef](#)]
20. Zhai, H.; Zhuo, F.; Zhu, C.; Yi, H.; Wang, Z.; Tao, R.; Wei, T. An optimal compensation method of shunt active power filters for system-wide voltage quality improvement. *IEEE Trans. Ind. Electron.* **2019**, *67*, 1270–1281. [[CrossRef](#)]
21. Teta, A.; Kouzou, A.; Rezaoui, M.M. Modeling and performance analysis of shunt active filter connected with photovoltaic system based on Z-source inverter. *COMPEL-Int. J. Comput. Math. Electr. Electron. Eng.* **2019**, *38*, 2001–2019. [[CrossRef](#)]
22. Zeng, Z.; Yang, H.; Zhao, R.; Cheng, C. Topologies and control strategies of multi-functional grid-connected inverters for power quality enhancement: A comprehensive review. *Renew. Sustain. Energy Rev.* **2013**, *24*, 223–270. [[CrossRef](#)]
23. Tareen, W.U.; Mekhilef, S.; Seyedmahmoudian, M.; Horan, B. Active power filter (APF) for mitigation of power quality issues in grid integration of wind and photovoltaic energy conversion system. *Renew. Sustain. Energy Rev.* **2017**, *70*, 635–655. [[CrossRef](#)]
24. Ravinder, K.; Bansal, H.O. Investigations on shunt active power filter in a PV-wind-FC based hybrid renewable energy system to improve power quality using hardware-in-the-loop testing platform. *Electr. Power Syst. Res.* **2019**, *177*, 105957. [[CrossRef](#)]
25. Mantilla, M.A.; Petit, J.F.; Ordoñez, G. Control of multi-functional grid-connected PV systems with load compensation under distorted and unbalanced grid voltages. *Electr. Power Syst. Res.* **2021**, *192*, 106918. [[CrossRef](#)]
26. Safa, A.; Berkouk, E.M.; Messlem, Y.; Gouichiche, A. A robust control algorithm for a multifunctional grid tied inverter to enhance the power quality of a microgrid under unbalanced conditions. *Int. J. Electr. Power Energy Syst.* **2018**, *100*, 253–264. [[CrossRef](#)]
27. Elnozahy, A.; Yousef, A.M.; Abo-Elyousr, F.K.; Mohamed, M.; Abdelwahab, S.A.M. Performance improvement of hybrid renewable energy sources connected to the grid using artificial neural network and sliding mode control. *J. Power Electron.* **2021**, *21*, 1166–1179. [[CrossRef](#)]
28. Deng, W.; Zhang, Y.; Tang, Y.; Li, Q.; Yi, Y. A neural network-based adaptive power-sharing strategy for hybrid frame inverters in a microgrid. *Front. Energy Res.* **2023**, *10*, 1082948. [[CrossRef](#)]
29. Bellia, H.; Youcef, R.; Fatima, M. A detailed modeling of photovoltaic module using MATLAB. *NRIAG J. Astron. Geophys.* **2014**, *3*, 53–61. [[CrossRef](#)]
30. Marmouh, S.; Boutoubat, M.; Mokrani, L. Performance and power quality improvement based on DC-bus voltage regulation of a stand-alone hybrid energy system. *Electr. Power Syst. Res.* **2018**, *163*, 73–84. [[CrossRef](#)]
31. Wu, B.; Lang, Y.; Zargari, N.; Kouro, S. *Power Conversion and Control of Wind Energy Systems*; John Wiley & Sons: Hoboken, NJ, USA, 2011.
32. Ma, Y.; Zhu, D.; Zhang, Z.; Zou, X.; Hu, J.; Kang, Y. Modeling and Transient Stability Analysis for Type-3 Wind Turbines Using Singular Perturbation and Lyapunov Methods. *IEEE Trans. Ind. Electron.* **2023**, *70*, 8075–8086. [[CrossRef](#)]
33. Cui, J.; Liu, S.; Liu, J.; Liu, X. A comparative study of MPC and economic MPC of wind energy conversion systems. *Energies* **2018**, *11*, 3127. [[CrossRef](#)]
34. Amir, M.; Srivastava, S.K. Analysis of mppt based grid connected hybrid renewable energy system with battery backup. In Proceedings of the 2018 International Conference on Computing, Power and Communication Technologies (GUCON), Greater Noida, India, 28–29 September 2018; IEEE: Piscataway, NJ, USA, 2018; pp. 903–907.
35. Narayana, M.; Putrus, G.; Jovanovic, M.; Leung, P.; McDonald, S. Generic maximum power point tracking controller for small-scale wind turbines. *Renew. Energy* **2012**, *44*, 72–79. [[CrossRef](#)]
36. Dali, A.; Abdelmalek, S.; Bakdi, A.; Bettayeb, M. A new robust control scheme: Application for MPP tracking of a PMSG-based variable-speed wind turbine. *Renew. Energy* **2021**, *172*, 1021–1034. [[CrossRef](#)]
37. Abd Rahim, N.; Selvaraj, J. Hysteresis current control and sensorless MPPT for grid-connected photovoltaic systems. In 2007 IEEE International Symposium on Industrial Electronics; IEEE: Piscataway, NJ, USA, 2007; pp. 572–577.
38. Al-Shetwi, A.Q.; Hannan, M.A.; Jern, K.P.; Alkahtani, A.A.; PGAbas, A.E. Power quality assessment of grid-connected PV system in compliance with the recent integration requirements. *Electronics* **2020**, *9*, 366. [[CrossRef](#)]
39. Varapasad, O.V.S.R.; Kumar, D.B.; Sarma, D.V.S.S.S. Three level hysteresis current controlled vsi for power injection and conditioning in grid connected solar pv systems. In Proceedings of the 2014 IEEE International Conference on Power Electronics, Drives and Energy Systems (PEDES), Mumbai, India, 16–19 December 2014; IEEE: Piscataway, NJ, USA, 2014; pp. 1–5.
40. Wai, R.-J.; Yang, Y. Design of backstepping direct power control for three-phase PWM rectifier. *IEEE Trans. Ind. Appl.* **2019**, *55*, 3160–3173. [[CrossRef](#)]

41. Youness, E.M.; Aziz, D.; Abdelaziz, E.G.; Jamal, B.; Najib, E.O.; Othmane, Z.; Khalid, M.; Bossoufi, B. Implementation and validation of backstepping control for PMSG wind turbine using DSPACE controller board. *Energy Rep.* **2019**, *5*, 807–821. [[CrossRef](#)]
42. El Mourabit, Y.; Derouich, A.; El Ghzizal, A.; El Ouanjli, N.; Zamzoum, O. Nonlinear backstepping control for PMSG wind turbine used on the real wind profile of the Dakhla-Morocco city. *Int. Trans. Electr. Energy Syst.* **2020**, *30*, e12297. [[CrossRef](#)]
43. Hoon, Y.; Mohd Radzi, M.A.; Hassan, M.K.; Mailah, N.F. DC-link capacitor voltage regulation for three-phase three-level inverter-based shunt active power filter with inverted error deviation control. *Energies* **2016**, *9*, 533. [[CrossRef](#)]
44. Barik, P.K.; Shankar, G.; Sahoo, P.K. Power quality assessment of microgrid using fuzzy controller aided modified SRF based designed SAPF. *Int. Trans. Electr. Energy Syst.* **2020**, *30*, e12289. [[CrossRef](#)]
45. Ali, T.; Mohamed Mounir, R.; Abdellah, K. Comparative Study of Different Control Strategies for Three-Phase Shunt Active Power Filter. In Proceedings of the 2018 IEEMA Engineer Infinite Conference (eTechNxT), New Delhi, India, 13–14 March 2018.

**Disclaimer/Publisher’s Note:** The statements, opinions and data contained in all publications are solely those of the individual author(s) and contributor(s) and not of MDPI and/or the editor(s). MDPI and/or the editor(s) disclaim responsibility for any injury to people or property resulting from any ideas, methods, instructions or products referred to in the content.